Materials Advances

ROYAL SOCIETY OF CHEMISTRY

PAPER

View Article Online
View Journal | View Issue

Cite this: *Mater. Adv.*, 2025, 6, 2253

Multifunctional oleic acid functionalized iron oxide nanoparticles for antibacterial and dye degradation applications with magnetic recycling

Shreya Sinha,[a] Rahul Sharma,[a] Mohd Rehan Ansari,[b] Rahul Singh,[a] Saurabh Pathak,*[c] Noor Jahan*[a] and Koteswara Rao Peta[b]

Nanotechnology that synchronously mitigates biomedical and environmental challenges is imperative for sustainable innovation. In this study, we report the synthesis of oleic acid (OA)-modified iron oxide (Fe_3O_4) nanoparticles *via* co-precipitation, which exhibit potent bactericidal effects and rapid photocatalytic dye degradation. Their intrinsic magnetic properties enable efficient recovery and repeated reuse, offering a robust platform for integrated remediation strategies. Comprehensive characterization confirmed that the synthesized OA-functionalized Fe_3O_4 nanoparticles (NPs) possess a single-phase cubic structure (12.17 nm crystallite size), an intact OA coating with particle size 13.01 nm, direct/indirect band gaps of 3.58/2.54 eV, and superparamagnetic behaviour exhibiting 40 emu g^{-1} saturation, confirming advanced functionality. The OA-coated Fe_3O_4 NPs exhibited a high zone of inhibition (ZOI) of 9.28 mm against *Escherichia coli* DH5α bacteria at a low concentration of 50 μg μL^{-1}, surpassing similar ferrite-based systems. The strong antibacterial activity is attributed to the generation of reactive oxygen species (ROS) and the controlled release of Fe^{2+}/Fe^{3+} ions, which disrupt the bacterial cell membrane, denature proteins, and damage DNA. The superparamagnetic nature of the NPs ensures minimal coercivity and remanence, facilitating precise targeting and magnetic separation in biomedical applications. Moreover, the OA-coated Fe_3O_4 NPs achieved 99.17% degradation of Rhodamine B (RhB) dye under visible light irradiation in 340 minutes. This performance is rooted in the synergistic effects of OA, which enhances light absorption and electron–hole pair separation, and Fe_3O_4, which drives redox reactions through its conduction band electrons and valence band holes. The photocatalytic degradation follows first-order kinetics, with a rate constant of 0.0079 min^{-1}. Importantly, the magnetic properties of the NPs allowed efficient recovery and reuse for four consecutive cycles, demonstrating long-term stability and economic viability. This study underscores the interplay between surface functionalization, magnetic behaviour, antimicrobial and catalytic properties, establishing OA-coated Fe_3O_4 NPs as a potent, cost-effective solution for dual-action biomedical and environmental applications.

Received 14th January 2025,
Accepted 5th March 2025

DOI: 10.1039/d5ma00036j

rsc.li/materials-advances

Introduction

Multifunctional materials are increasingly central to advancements in materials science, offering a unified solution to complex challenges spanning biomedicine, environmental protection, energy storage, and catalysis.[1–4] These materials combine diverse properties such as mechanical robustness, magnetic responsiveness, optical activity, and chemical stability, enabling their integration into various high-performance applications.[5–7] Their development aligns with the growing demand for environmentally sustainable and technologically efficient solutions.[8,9] Among these, magnetic nanoparticles (MNPs) have garnered notable attention due to their high surface area-to-volume ratio, unique magnetic properties, and adaptable surface chemistry, enabling precise tuning for targeted uses.[10–12]

Iron oxide (Fe_3O_4) NPs exemplify this class of materials, distinguished by their biocompatibility, superparamagnetic behaviour, and amenability to functionalization.[10,13–15] Their ability to toggle between ferrimagnetic and superparamagnetic phases, governed by size (~10–25 nm) and thermal conditions, makes them ideal candidates for biomedical and environmental applications.[16–18] Additionally, Fe_3O_4 NPs exhibit significant

[a] *Department of Physics and Astronomical Sciences, Central University of Himachal Pradesh, Dharamshala, Kangra, HP, 176215, India. E-mail: noor.jahan@hpcu.ac.in*
[b] *Department of Electronic Science, University of Delhi South Campus, New Delhi, 110021, India*
[c] *National Creative Research Center for Spin Dynamics and SW devices, Department of Material Sciences and Engineering, Seoul National University, Seoul 151-744, South Korea. E-mail: pathak@snu.ac.kr*

magnetic anisotropy and high saturation magnetization, which are desirable for targeted therapies, hyperthermia treatments, and catalytic activities.[15,17,19,20] Surface functionalization—frequently achieved with coatings like oleic acid (OA)—further improves their stability, mitigates agglomeration caused by van der Waals forces and magnetic dipole interactions, and enhances their functional versatility.[3,21–23] MNPs exhibit bifunctional efficacy in both countering antimicrobial resistance and catalysing the remediation of environmental pollutants, thereby solidifying their central role in advanced material science. Their inherent magnetic, catalytic, and surface-active properties, further enhanced through precise nano structural engineering and surface functionalization, enable the fine-tuning of synergistic interactions that bolster both bactericidal activity and contaminant degradation. This study rigorously investigates OA-functionalized Fe_3O_4 MNPs, delineating their potential as sustainable, cost-effective nanoplatforms for integrated biomedical and environmental applications.

The rising prevalence of antibiotic-resistant pathogens underscores the urgent need for innovative antimicrobial strategies.[24] MNPs, particularly iron oxide-based systems, offer a promising approach due to their ability to generate reactive oxygen species (ROS) and release metal ions capable of disrupting microbial integrity.[25] The antibacterial mechanism of Fe_3O_4 NPs is deeply rooted in their surface charge, size, and functionalization, all of which influence their interaction with negatively charged bacterial membranes.[26,27] The production of ROS, primarily hydroxyl radicals ($^{\bullet}OH$), is the underpinning of the antibacterial efficacy of these systems. This is facilitated through a Fenton-like reaction, where iron ions (Fe^{2+}/Fe^{3+}) catalyse the decomposition of hydrogen peroxide (H_2O_2). The Fenton reaction ($Fe^{2+} + H_2O_2 \rightarrow Fe^{3+} + {}^{\bullet}OH + OH^-$) and the Haber–Weiss reaction ($Fe^{3+} + H_2O_2 \rightarrow Fe^{2+} + {}^{\bullet}OOH + H^+$) generate highly reactive $^{\bullet}OH$ and other ROS.[28] These potent oxidants readily attack critical cellular components, including lipids in the bacterial membrane, leading to lipid peroxidation and membrane disruption. Furthermore, ROS can oxidize proteins, inactivating essential enzymes and disrupting cellular functions.[29–31] Additionally, they can damage nucleic acids, causing DNA strand breaks and inhibiting DNA replication and transcription. The release of Fe^{2+} and Fe^{3+} ions from the NPs can also disrupt bacterial homeostasis by interfering with ion transport across the cell membrane and disrupting cellular metabolism. Functionalization with OA enhances the dispersibility of the NPs in aqueous media, ensuring consistent interaction with microbial surfaces and maximizing their antimicrobial efficacy.[23]

Numerous studies have explored the antibacterial properties of MNPs. For instance, Ansari *et al.* have synthesized $ZnFe_2O_4$ NPs *via* co-precipitation method, achieving a zone of inhibition (ZOI) of 5.30 mm against *Escherichia coli* at 50 μg μL^{-1}.[26] Similarly, Hatami *et al.* have synthesized $CuFe_2O_4$ and $ZnFe_2O_4$ NPs *via* co-precipitation route and have reported ZOI values of 12 mm and 27 mm, respectively, under comparable conditions.[32] In an analogous study, Naik *et al.* reported a 6 mm ZOI for $NiFe_2O_4$ NPs prepared *via* the sol–gel autocombustion method.[33] Further, $MnFe_2O_4$ NPs demonstrated a ZOI of 6.2 mm when annealed at 500 °C *via* hydrothermal method.[34] Furthermore, $CdFe_2O_4$ NPs demonstrated a ZOI of 12 mm, while $CoFe_2O_4$ NPs achieved a ZOI of 14 mm at a concentration of 8 μg μL^{-1} under similar conditions.[35] Ikram *et al.* reported the ZOI of 3.55 mm and 4.60 mm at a concentration of 0.5 mg/50 μL and 1 mg/50 μL for Sr/St doped Fe_2O_3 nanorods.[36] In another captivating study, functionalized Fe_3O_4 NPs exhibited a ZOI of 2 cm at a concentration of 100 μg mL^{-1}, surpassing many other ferrite-based systems.[37] These results underscore the significance of surface functionalization, with OA-coated Fe_3O_4 NPs frequently demonstrating superior activity due to enhanced ROS generation and metal ion release.

In addition to their antibacterial applications, MNPs play a crucial role in environmental remediation applications. Photocatalysis, an eco-friendly method for degrading organic pollutants, has advanced significantly with the integration of MNPs.[38–40] Fe_3O_4, functionalized with materials such as OA, serve as efficient photocatalysts by promoting the generation of electron–hole pairs under visible light irradiation. The excitation of electrons from the valence band (VB) to the conduction band (CB) leaves holes in the VB, enabling redox reactions crucial for pollutant degradation. These mechanisms are represented as: $Fe_3O_4 + h\nu \rightarrow Fe_3O_4\ (e^- + h^+)$; $h^+ + H_2O \rightarrow {}^{\bullet}OH$ and $e^- + O_2 \rightarrow {}^{\bullet}O_2^-$. The resultant $^{\bullet}OH$ and superoxide anions ($^{\bullet}O_2^-$) exhibit potent oxidative capabilities, breaking down complex organic molecules into benign products like CO_2 and H_2O.[41] OA surface functionalization mitigates NPs agglomeration, thereby augmenting the effective surface area and curtailing electron–hole recombination. This enhanced dispersion facilitates optimal interfacial contact between the photocatalyst and target pollutants, resulting in superior degradation kinetics.

Extensive studies have investigated the photocatalytic potential of MNPs for degrading various organic pollutants. For example, SiO_2-coated Fe_3O_4 NPs demonstrated a degradation efficiency of over 97% for Rhodamine B under visible light irradiation.[42] Similarly, TiO_2-modified systems have shown high photocatalytic activity, primarily due to enhanced charge separation and increased ROS production.[43] $ZnFe_2O_4$ NPs achieved an impressive degradation efficiency of 97.5% for Rhodamine B, highlighting their rapid catalytic performance.[44] In another study, Zn-doped Fe_3O_4 NPs exhibited a degradation efficiency of 97.31% against Rhodamine B within 300 minutes.[45] Furthermore, the incorporation of co-catalysts such as Ag or Pt has been shown to improve electron–hole pair separation, significantly enhancing the photocatalytic degradation rates. Reusability is a pivotal advantage of MNPs in photocatalysis. Their superparamagnetic properties facilitate efficient recovery and reuse, with minimal performance loss over multiple cycles. Gupta *et al.* evaluated the stability of $NiFe_2O_4$ photocatalysts over seven consecutive cycles, observing only a minimal 6.0% loss in photodegradation efficiency after the seventh cycle. This underscores the high durability and reusability of these photocatalysts, making them ideal for extended applications.[40] Similarly, Miao *et al.* demonstrated the recyclability of Ni-doped Fe_3O_4 NPs over five

consecutive cycles, with no significant loss in performance.[42] Tony *et al.* further showcased the exceptional stability of $Mn_{0.6}Zn_{0.4}Fe_2O_4$ ferrites, which retained their photocatalytic efficiency across eight consecutive cycles.[43] These studies highlight the robust reusability of MNPs, making them promising candidates for sustainable photocatalytic applications. Additionally, the inclusion of H_2O_2 as a co-catalyst significantly enhances $^{\bullet}OH$ production, accelerating pollutant degradation.[46] The integration of magnetic properties, high stability, and visible light responsiveness positions Fe_3O_4 NPs as a sustainable solution for environmental remediation. Their dual capability in antibacterial and photocatalytic applications exemplifies their multifunctionality, making them indispensable in addressing critical global challenges. Despite the extensive body of research on iron oxide NPs, there remains a need to systematically investigate the synergistic effects of surface functionalization on their multifunctional properties. Studies have demonstrated the role of coatings such as silica, and OA in enhancing stability and activity, yet a unified framework connecting these findings is lacking.

This study focuses on the synthesis, characterization, and application of OA-coated Fe_3O_4 NPs for antibacterial and photocatalytic applications. The NPs were synthesized using a co-precipitation method, chosen for its operational simplicity, scalability, and environmental compatibility. This method facilitates the simultaneous precipitation of ferric and ferrous ions under alkaline conditions, yielding magnetite NPs with high purity and reproducibility. Subsequently, they were surface-modified with OA to enhance their stability, dispersibility, and compatibility in various environments. Structural properties were thoroughly analysed using X-ray diffraction (XRD), supported by Rietveld refinement to determine phase purity, crystallite size, and lattice strain. Morphological features were examined using high-resolution electron microscopy, revealing uniform particle distribution and surface characteristics. The optical properties of the NPs were evaluated through UV-vis spectroscopy, demonstrating their potential for light-driven catalytic processes, while FTIR analysis confirmed the successful functionalization of Fe_3O_4 with OA by identifying characteristic vibrational modes. Magnetic properties were investigated using a vibrating sample magnetometer (VSM), where the magnetization data were modelled using Langmuir and LAS function fittings to provide insights into their superparamagnetic behaviour and saturation magnetization. The study explores the dual functionality of OA-coated Fe_3O_4 NPs in antibacterial and photocatalytic applications. The antimicrobial efficacy was assessed against pathogenic bacteria, highlighting their potential as an effective antibacterial agent. Simultaneously, photocatalytic activity was demonstrated through the degradation of organic pollutants under visible light, showcasing their ability to act as a sustainable solution for environmental remediation. By integrating comprehensive structural, optical, and magnetic characterizations, this work establishes OA-coated Fe_3O_4 NPs as a promising material for multifunctional applications while maintaining focus on the primary objectives.

Experiment

Materials

The ferrous sulfate heptahydrate [$FeSO_4{\cdot}7H_2O$], ferric sulfate hydrate [$Fe_2(SO_4)_3{\cdot}xH_2O$], oleic acid [$C_{18}H_{34}O_2$] and ammonia solution [NH_4OH] were used as precursor materials and were purchased from Thermo Fisher Scientific Pvt. Ltd. All chemicals were used as received. Type I distilled water ($\sim$18.2 MΩ cm^{-1}) was used in the synthesis process for making the aqueous solution.

Synthesis of OA-coated Fe_3O_4

The synthesis of OA-coated Fe_3O_4 NPs was carried out using a modified co-precipitation technique. The synthesis adheres to a stringent Fe^{3+}/Fe^{2+} stoichiometric ratio of 2 : 1, imperative for phase-pure Fe_3O_4 formation. Ferric sulfate hydrate and ferrous sulfate heptahydrate were dissolved in deionized water to yield a homogeneous precursor solution, wherein OA, functioning as a capping and stabilizing ligand, was introduced to mitigate agglomeration and enhance colloidal stability. The functionalization process is primarily driven by the interaction between the carboxylic (–COOH) group of OA and the iron atoms on the nanoparticle surface. This chemical bonding imparts a robust organic coating that stabilizes the Fe_3O_4 core. The hydrophobic alkyl chain of OA provides steric hindrance, mitigating magnetic dipole–dipole interactions and van der Waals forces, which are major contributors to nanoparticle agglomeration. This dual role of OA not only ensures the NPs long-term stability in dispersion but also significantly influences their physicochemical properties, such as magnetic responsiveness and surface reactivity. 4 mL of OA was added under vigorous stirring at an elevated temperature of 80 °C. This temperature was chosen to optimize the solubility of the reagents, promote uniform interaction of OA with nascent NPs, and facilitate surface functionalization. Ammonia solution (NH_4OH) was then added dropwise to the precursor mixture until a pH of $\sim$11 was achieved. At this alkalinity, hydroxyl ions catalysed the nucleation and growth of Fe_3O_4 NPs. The black precipitate, indicative of Fe_3O_4 formation, was separated using magnetic decantation to minimize contamination and ensure high yield. The precipitate was subjected to iterative washing with DI water to remove excess OA, ammonia, and other reaction byproducts. This step is critical for achieving phase purity and optimal surface chemistry. The purified NPs were dried overnight in an oven at 70 °C to remove residual moisture, followed by gentle grinding using an agate mortar and pestle. This ensured the production of a fine, uniform powder suitable for further characterization and applications.

Antibacterial assay

In order to evaluate the antibacterial activity of Fe_3O_4 NPs, agar well diffusion method was employed as explained by Diogo *et al.*[41] against the Gram-negative bacteria *Escherichia coli* (*E. coli*) DH5α strain of bacteria. The method is carried out by dissolving different concentrations such as 25 μg μL^{-1} and 50 μg μL^{-1} of Fe_3O_4 in dimethyl sulfoxide (DMSO) and

sterilized using UV radiation and filtration. The media plate was made by pouring sterilized Luria broth (LB) agar in the Petri plate and allowed it to solidify. A matured *E. coli* bacterial culture was uniformly distributed onto the solidified agar plate. Subsequently, the wells were drilled into the agar plate by using sterilized steel cork borers. The different concentration of Fe_3O_4 NPs as mentioned above with antibiotic (positive control) and the solvent (negative control) poured into the well to test the antibacterial properties. The plates were placed into the incubator for 24–36 hours at 37 °C. The size of zones around the wells were noted after 24–36 hours, which reflects the antibacterial properties of the Fe_3O_4 NPs in comparison with the known standard antibiotic.

Photocatalytic degradation experiment

To investigate the photocatalytic activity of OA-coated Fe_3O_4 NPs, RhB dye, a commonly used model pollutant, was selected for degradation experiments. For this, 50 mg sample of the OA-coated Fe_3O_4 NPs was mixed with the 50 mL RhB dye solution of 10 ppm concentration. The adsorption–desorption equilibrium was achieved by first keeping the solution in dark for 30 minutes. Then, it was exposed to the visible light source (200 W Tungsten lamp, $\lambda > 420$ nm) to initiate the photocatalytic degradation phenomenon. To enhance the photocatalytic activity, the desired amount of H_2O_2 was added to the solution and stirred magnetically throughout the experiment to ensure uniform mixing. After a regular time interval, 3 mL of the solution was withdrawn, centrifuged and the supernatant was analysed *via* UV-vis spectrophotometer at a wavelength of 554 nm which is characteristic of the RhB dye. The degradation experiment was carried out for duration of 340 minutes and photocatalytic degradation efficiency was calculated by using the formula, as follows:

$$\text{Degradation } (\%) = \frac{C_0 - C_t}{C_0} \times 100 \quad (1)$$

where C_0 and C_t are the initial concentration of RhB dye and final concentration at time 't'.

Characterization techniques

The Bruker D8 Advance was utilised to obtain X-ray diffraction pattern over a 2θ range of 10° to 80° at a scan rate of 2° min^{-1}, using Cu-Kα radiation of X-ray source. Fourier Transform Infrared Spectroscopy (FTIR) was employed to identify the functional groups within the material by examining their characteristic vibrational fingerprints. The spectra were recorded using the model Thermo Scientific Nicolet iS20 between range 500 to 4000 cm^{-1}. The band gap of the material was estimated *via* UV-vis spectrophotometer (Thermo Scientific Genesys 180). The samples were analysed in a quartz cell and ultrapure distilled water (Type 1) was used as the reference solvent. The transmission electron microscopy (TEM) images and selected area electron diffraction (SAED) pattern were acquired using the model TECNAI G2 20 S-TWIN at 200 kV to analyse the microstructures of the sample. An ADE-EV9 vibrating sample magnetometer (VSM) was used to investigate the magnetic properties of the material with maximum applied magnetic field of ±10 kOe.

Results and discussion

Crystallographic analysis of OA-coated Fe_3O_4 NPs

The crystalline structure of OA-coated Fe_3O_4 NPs was elucidated using X-ray diffraction (XRD) analysis. The diffraction patterns (Fig. 1a) revealed characteristic Bragg reflection peaks at 18.32°, 30.18°, 35.50°, 37.22°, 43.15°, 53.54°, 57.07°, 62.67°, and 74.39°, corresponding to the (111), (220), (311), (222), (400), (422), (511), (440), and (531) crystal planes. These peaks confirm the formation of a single-phase cubic spinel structure of Fe_3O_4, with no detectable impurities or secondary phases. The predominant (311) peak aligns with the established diffraction pattern for Fe_3O_4, indicative of its high crystallinity and phase purity. The average size (D) was determined using the Debye–Scherrer equation: $D = k\lambda/\beta_{hkl}\cos\theta$, where k is the Scherrer constant (0.9 for cubic systems), λ represents the X-ray wavelength ($\sim$1.54 Å for Cu-Kα radiation), β is the full-width at half-maximum (FWHM) of the diffraction peak in radians, and θ is the Bragg angle.[47,48] The calculated average crystallite size was approximately 12.17 nm. This nanoscale crystallinity plays a pivotal role in dictating the magnetic and catalytic properties of the NPs, making them suitable for multifunctional applications. The lattice parameter (a) was calculated using the interplanar spacing equation for cubic systems: $a = \lambda\frac{\sqrt{h^2+k^2+l^2}}{2\sin\theta}$ where h, k, l are the Miller indices of the most intense peak (311).[4,49] The derived lattice parameter was 8.3740 Å, in excellent agreement with the standard value for Fe_3O_4. Further, the unit cell volume (V) and X-ray density (d_x) were calculated using the following relationships: $d_x = \frac{ZM}{N_A(a^3)}$ and $V = a^3$.[50,51] Here, Z is the number of formula units per unit cell (8 for Fe_3O_4), M is the molecular weight of Fe_3O_4, and N_A is Avogadro's number. The calculated values, including d_x = 11.7006 g cm^{-3}, are presented in Table 1. Dislocation density (δ) and surface area (S.A.) were computed using the following formulae:[52]

$$\delta = \frac{1}{D^2} \quad (2)$$

$$\text{S.A.} = \frac{6}{d_x \times D} \quad (3)$$

These metrics, listed in Table 1, provide insights into structural imperfections and surface reactivity, crucial for tuning the material's functionality. Rietveld refinement of the powder XRD data was conducted using the Fullprof software to determine precise structural parameters. The refinement procedure utilized the Thompson–Cox–Hastings pseudo-Voigt function, incorporating axial divergence effects. Iterative adjustments were made to refine parameters such as scale factor, background, atomic occupancies, and instrumental broadening. (Fig. 1a) illustrates the results of the Rietveld refinement. An excellent goodness-of-fit value (χ^2 = 1.01) was obtained, confirming the

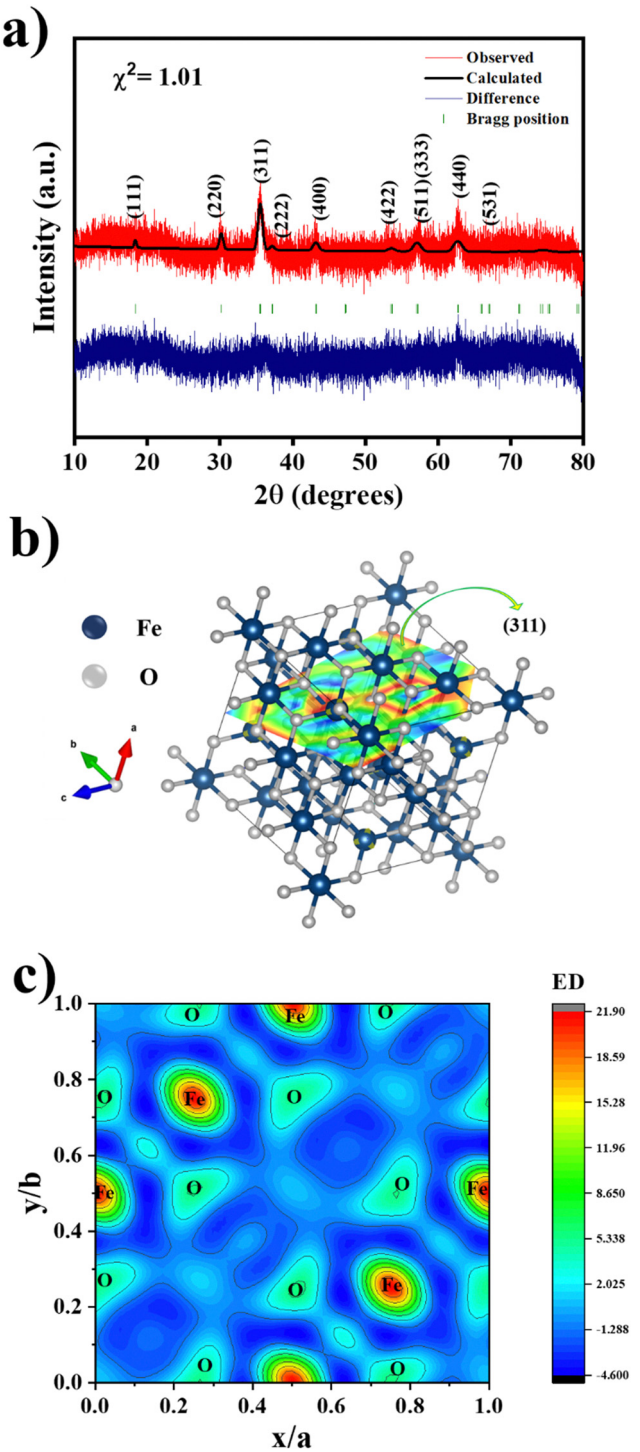

Fig. 1 (a) Rietveld refinement analysis of OA-coated Fe_3O_4 NPs, (b) Crystal structure of OA-coated Fe_3O_4 NPs with the (311) crystal plane highlighted, and (c) electron density map showcasing atomic distribution.

reliability of the structural model. The refinement confirmed that Fe_3O_4 crystallizes in a cubic phase with the space group $Fd\bar{3}m$ (no. 227) and lattice parameters of $a = b = c = 8.3781$ Å. Table 1 summarizes the refined structural parameters. (Fig. 1b) depicts the crystal structure of Fe_3O_4 visualized using the VESTA software. The structure was derived from the Rietveld analysis, and the figure highlights the (311) crystal plane, corresponding to the most intense peak in the diffraction pattern. (Fig. 1c) displays a Fourier transform map that visually depicts the electron density distribution (EDD) within the material. By analyzing the EDD, we can gain valuable insights into the positions of atoms, the nature of the bonds between them (covalent, ionic, *etc.*), and how the electrons are distributed within these bonding regions. Here, red color represents a high electron density region whereas fluorescent green color represents a low-energy density region. The closed shell contours followed by low electron density region indicate the predominant ionic bonding nature.[53]

Optical properties: FTIR and UV-vis spectroscopy

Fourier transform infrared (FTIR) spectroscopy was utilized to confirm the functionalization of Fe_3O_4 NPs with OA and to investigate the vibrational modes associated with the synthesized sample. The FTIR spectrum (Fig. 2a) displayed several characteristic peaks indicative of both the magnetite core and the OA coating. The prominent absorption band at 564 cm^{-1} corresponded to the Fe–O stretching vibration in the tetrahedral sites of the Fe_3O_4 spinel structure, confirming the formation of magnetite.[54] This peak, being a fingerprint of Fe_3O_4, establishes the crystalline integrity of the core material. The OA coating was confirmed by characteristic peaks associated with the carboxylate group ($-COO^-$). The peaks at 1530 cm^{-1} and 1424 cm^{-1} were attributed to asymmetric and symmetric stretching vibrations of $-COO^-$, indicating the chemical binding of OA to the NPs surface.[14,55] The presence of peaks at 2917 cm^{-1} and 2849 cm^{-1}, corresponding to asymmetric and symmetric stretching of CH_2 groups, confirmed the hydrocarbon chain of OA.[56–58] These assignments are consistent with the reported literature, providing quantitative evidence of the effective functionalization. Additionally, a broad band between 3000–3500 cm^{-1} was observed, attributed to O–H stretching vibrations from adsorbed water or surface hydroxyl groups.[57–60] The peak at 1709 cm^{-1} was assigned to the C=O stretching vibration of unbound OA, potentially due to storage conditions. Samples were dried prior to measurement to minimize moisture; however, due to moderate thermal treatment (90–95 °C) rather than high-temperature annealing, residual moisture adsorption occurred. Consequently, the broad FTIR band reflects contributions from both adsorbed water and unbound OA, including unreacted molecules with polar heads that interact with ambient moisture. A similar observation has been reported in previous literature,[60,61] further validating its presence in the spectra. These FTIR results establish the dual role of OA as a surface stabilizer and dispersant, preventing aggregation of the NPs and enhancing their colloidal stability in solution. To further analyze the bonding strength between the metal and oxygen ions in the Fe_3O_4 structure, the force constant (K) was calculated using the following relationship:

$$K = 4\pi^2 c^2 \nu^2 m \quad (4)$$

Here, c is the speed of light ($\sim 3 \times 10^8$ m s^{-1}), ν is the vibrational frequency (in cm^{-1}) associated with the Fe–O bond

Table 1 Crystallographic parameters of OA-coated Fe_3O_4 NPs

	D (nm)						Rietveld refined parameters					
								Atomic positions				
Sample	D–S	$a = b = c$ (Å)	V (Å^3)	d_x (g cm^{-3})	δ ($\times 10^{15}$ m^{-2})	S.A.	Atoms	x	y	z	Occupancy	Strain
OA-coated Fe_3O_4	12.17	8.3740	583.8	11.7006	6.75	42.23	FeT	0.125	0.125	0.125	0.04167	0.5940
							FeM	0.500	0.500	0.500	0.08333	
							O	0.255	0.255	0.255	0.16667	

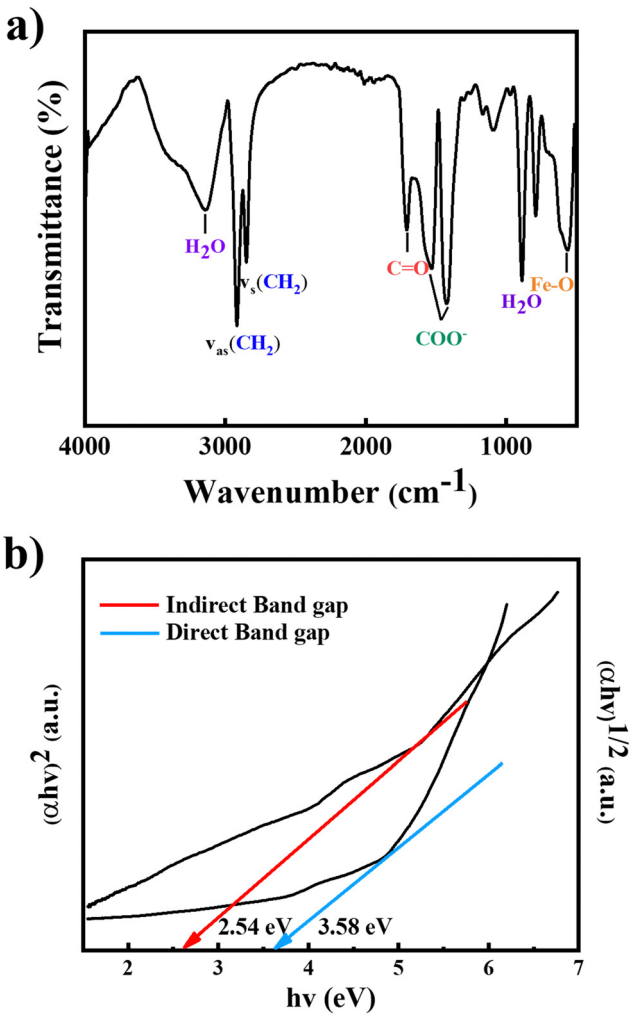

Fig. 2 (a) FTIR spectra of OA-coated Fe_3O_4 NPs, (b) Tauc plot for direct and indirect band gap energy of OA-coated Fe_3O_4 NPs.

(calculated from 564 cm^{-1}), and m is the reduced mass of the Fe and O atoms, given by: $m = m_{Fe} \times m_O/(m_{Fe} + m_O)$. Using atomic masses of iron (55.85 g mol^{-1}) and oxygen (16.00 g mol^{-1}), the reduced mass was determined to be 2.065×10^{-23} g. Substituting these values, the force constant for the Fe–O bond was calculated to be $K = 2.328$ N cm^{-1}. This high force constant reflects the strong ionic bonding within the magnetite structure, contributing to its thermal and structural stability.

UV-Vis spectroscopy was employed to investigate the optical absorption properties of the OA-coated Fe_3O_4 NPs within the wavelength range of 200–800 nm at room temperature. The spectra (Fig. 2b) exhibited a maximum absorption peak between 200–204 nm which is close to the reported wavelengths of around 233 nm and 250 nm indicating the successful formation of Fe_3O_4 NPs.[62] The band gap energy values for the synthesized sample can be calculated by using Kubelka–Munk equation and were evaluated by plotting Tauc plot using the equation:

$$(\alpha h\nu)^n = (h\nu - E_g) \quad (5)$$

here α is the absorption coefficient which relates a material's ability to absorb light (A) to the thickness (t) of the cuvette ($\alpha = 2.303$ A t^{-1}), h is the Planck's constant, ν is the photon's frequency, n is the order of electron transition and E_g is the band gap energy. The Tauc plot method was used to determine material's optical direct and indirect band gap energies. For indirect band gaps, the plot utilized $(\alpha h\nu)^{1/2}$ and $h\nu$ while for the direct band gap, the $(\alpha h\nu)^2$ was plotted against photon energy. The linear portion was then extrapolated to the x-axis (energy equal to zero) which corresponds to the optical direct and indirect band gap respectively of OA-coated Fe_3O_4 NPs as depicted in (Fig. 2b). The estimated band gap energies (3.58 eV for direct and 2.54 eV for indirect) fall within the range reported in the literature.[63,64]

Morphology of OA-coated Fe_3O_4 NPs

Fig. 3 illustrate high-resolution transmission electron microscopy (HR-TEM) images of the synthesized OA-coated Fe_3O_4 NPs, demonstrating their uniform spherical morphology, surface coating and well-dispersed nature. The observed isolation of individual NPs (Fig. 3a) is attributed to the steric repulsion provided by the OA coating, effectively counteracting the van der Waals forces that typically promote agglomeration.[65] Using ImageJ software, the particle size was quantified and found to have an average diameter of ~13.01 nm, as determined from the corresponding histogram analysis (shown in inset of Fig. 3a). A higher magnification image (5 nm scale) provided in (Fig. 3b) further highlights the uniformity and structural integrity of the NPs. The TEM images (Fig. 3b) confirm that the OA coating forms a uniform layer around the NPs, minimizing aggregation and enhancing dispersion. This improved dispersion increases the availability of reactive surfaces, facilitating efficient bacterial trapping and interaction in antibacterial applications while also promoting enhanced light absorption and charge separation in photocatalysis. Comparable high-resolution images have also been presented in previous studies which support our findings.[59,66,67] Also, the inset of the figure

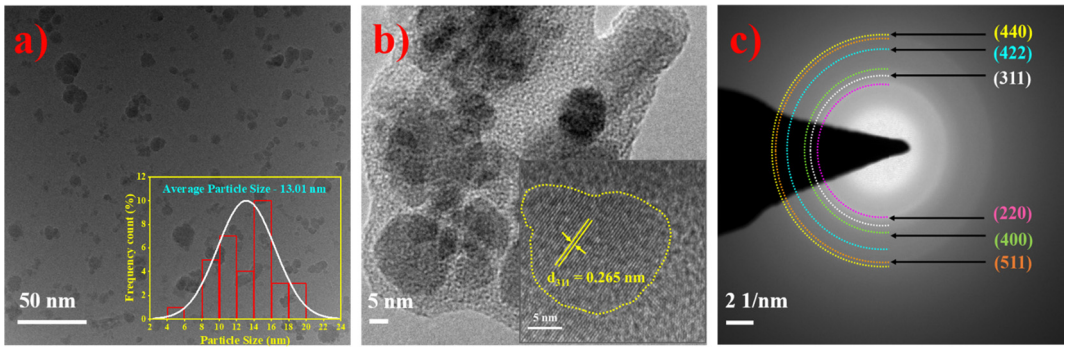

Fig. 3 (a) TEM micrograph of the OA-coated Fe_3O_4 NPs with the inset showing the particle size distribution histogram, (b) HRTEM image of the NPs showing OA coating on NPs. Inset of the figure shows the lattice spacing corresponding to (311) plane. (c) SAED pattern illustrating multiple solid rings indicating polycrystalline nature of the NPs.

shows the lattice spacing of 0.265 nm which is associated with the (311) planes of the spinel ferrites. The selected area electron diffraction (SAED) pattern (Fig. 3c) reveals a series of well-defined distinct concentric bright rings, confirming the polycrystalline nature of the Fe_3O_4 NPs. These rings correspond to the diffraction from multiple crystallographic planes, indicative of the long-range periodicity within the nanostructure. The observed diffraction pattern aligns with prior studies by Shete *et al.*,[68] reinforcing the structural integrity and phase purity of the synthesized Fe_3O_4 NPs. Additionally, the indexed reflection planes in the SAED pattern exhibit excellent agreement with the X-ray diffraction (XRD) data, affirming the crystallographic structure of the synthesized material.

Magnetic measurement using vibrating sample magnetometry

Fig. 4 illustrates the hysteresis behavior of the OA-coated Fe_3O_4 NPs, as measured using vibrating sample magnetometry (VSM) under an applied magnetic field ranging from −10 kOe to +10 kOe. The magnetization (M) *versus* applied magnetic field (H) curve (Fig. 4a) exhibits a well-saturated s-shaped profile with negligible coercivity (H_c) and remanent magnetization (M_r), as highlighted in the inset. These characteristics confirm the superparamagnetic nature of the synthesized NPs, attributed to their average size lower to that of the critical size, as supported by structural and morphological analyses.[52] Additionally, the M–H curve was fitted with the Langevin equation (Fig. 4a, red line), further corroborating the superparamagnetic behavior of the Fe_3O_4 NPs. The absence of significant hysteresis underscores the suitability of these NPs for applications requiring rapid magnetic response without residual magnetization.[52] The M–H curve was fitted with the Langevin function using eqn (6) (Fig. 4a, red line), further validating the superparamagnetic behaviour of the Fe_3O_4 NPs.

$$M(H) = M_s L\left(\frac{\mu_0 H}{kT}\right) + \chi H \qquad (6)$$

Here, M_s is the saturation magnetization, $L\left(\frac{\mu_0 H}{kT}\right)$ is the Langevin function a ratio of magnetic to the thermal energy, χ is defined by the magnetic susceptibility and H is the applied

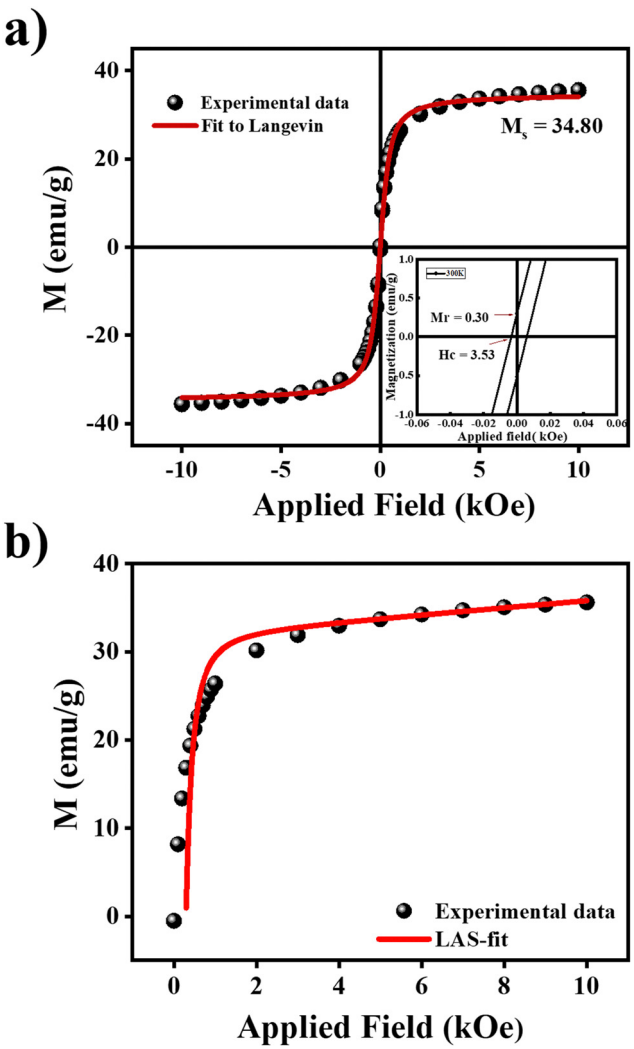

Fig. 4 (a) Room temperature M–H curve of the OA-coated Fe_3O_4 NPs with a Langevin function fit, confirming their superparamagnetic behavior. The inset provides an enlarged view of the M–H curve near the origin, highlighting the negligible coercivity and remanence. (b) LAS fit of the M–H curve, further validating the magnetic characteristics and saturation magnetization of the NPs.

Table 2 Magnetic parameters obtained from M–H curve of OA-coated Fe_3O_4 NPs

	M_s values (in emu g^{-1})					
Sample	LAS-fit	Langevin-fit	M_r (emu g^{-1})	S	b	X_f (emu g^{-1} Oe^{-1})
OA-coated Fe_3O_4	32.35	34.81	0.30	0.009	8.76×10^4	3.96×10^{-4}

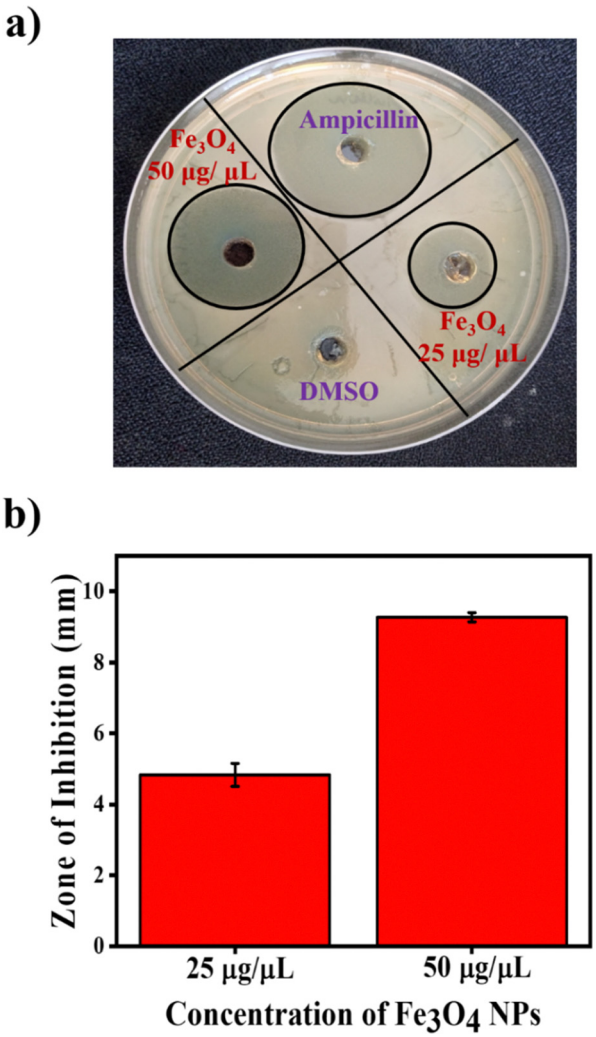

Fig. 5 (a) Antibacterial activity of the OA-coated Fe_3O_4 NPs at different concentrations using agar well diffusion method on *E. coli* DH5α strain of bacteria. (b) Error-bar graph representing the ZOI (in mm) at various sample concentrations.

magnetic field. The high correlation of the experimental data with the Langevin function fit underscores the robust superparamagnetic properties of the OA-coated Fe_3O_4 NPs, highlighting their suitability for applications requiring rapid magnetic response and negligible hysteresis. The saturation magnetization of the OA-coated Fe_3O_4 NPs was determined to be 34.80 emu g^{-1}, significantly lower than the bulk Fe_3O_4 value ($\sim$80 emu g^{-1}). This reduction is attributed to the increased surface-to-volume ratio and dimensional confinement inherent to the nanoscale regime, which results in suppressed magnetic interactions and surface spin canting. Furthermore, the average particle size of $\sim$13 nm, as calculated from morphological analysis, supports the superparamagnetic behaviour without magnetic domain formation, consistent with the characteristics reported by Pathak *et al.*[69–71] (Fig. 4b) depicts the fit of the magnetization curve using the law of approach to saturation (LAS) as described by the following equation:

$$M(H) = M_s\left(1 - \frac{b}{H^2}\right) + \chi_f H \quad (7)$$

$$\text{where,} \quad b = \frac{8}{105}\frac{K_1^2}{\mu_0^2 M_s^2} \quad (8)$$

Here, K_1 is defined by the cubic anisotropy constant and χ_f is known as the high field susceptibility. The constants such as b, χ_f are determined by fitting. The value of K_1 is obtained from eqn (8) (3.7×10^4 erg cm^{-3}).[68] Furthermore, the squareness ratio (S), defined as $= \frac{M_r}{M_s}$, was found to be less than 1. This observation underscores the suitability of the OA-coated Fe_3O_4 NPs for biomedical applications, where low coercivity and remanence are advantageous. In contrast, a higher squareness ratio is typically required for memory storage device applications.[72] The extracted values for b, χ_f, M_r, M_s and S, are presented in Table 2.

Antibacterial activity

The agar well diffusion method was employed to assess the antibacterial efficacy of Fe_3O_4 NPs against *E. coli* DH5α, a Gram-negative bacterium. The ZOI created around the well was measured and compared with the known antibiotic ampicillin. The diameter of the created zones defines the potential of the

Table 3 Comparison of Fe_3O_4 NPs with other ferrite materials for antibacterial property

S. no.	Ferrite NPs	Concentration	Bacteria	ZOI (mm)	Ref.
1	$CuFe_2O_4$	600 µg $µL^{-1}$	*E. coli*	12.0 (± 0.9)	32
2	$NiFe_2O_4$	100 µg mL^{-1}	*E. coli*	6	33
3	$CoFe_2O_4$	100 µg $µL^{-1}$	*E. coli*	—	73
4	$ZnFe_2O_4$	50 µg $µL^{-1}$	*E. coli* DH5α	5.30 (± 0.6)	26
5	OA-coated Fe_3O_4	25 µg $µL^{-1}$	*E. coli* DH5α	4.83 (± 0.32)	[Present study]
		50 µg $µL^{-1}$		9.28 (± 0.13)	

NPs. The different concentrations of NPs such as 25 μg μL^{-1} and 50 μg μL^{-1} have been taken for the test with ampicillin (antibiotic) as a negative control and DMSO as a positive control shown in Fig. 5a. The average diameter of the ZOI for the Fe_3O_4 NPs is 4.83 mm (at 25 μg μL^{-1}) and 9.28 mm (at 50 μg μL^{-1}), respectively (shown in Fig. 5b). The results showed that as the concentration of NPs increased, the ZOI also increased, indicating dose-dependent inhibition. Table 3 shows the comparison of ZOI of different studies for different NPs.

The bactericidal effect exhibited by OA-coated Fe_3O_4 NPs is attributed to their small size and increased surface to volume ratio as described by Dabagh *et al.* and others.[26,27] Heavy metal ion release and ROS production are two key elements that determine the effectiveness of the NPs.[25] The heavy metal ions Fe^{2+} and Fe^{3+} were released by Fe_3O_4 NPs and these positive ions attached to the negatively charged bacteria surface, thus creating disturbance at the outer cell membrane of microbe.[42] After entering into the cell, these ions damage the cellular organelles, which involves cell division, cellular respiration and DNA replication. Thus, ROS produced inside the cell due to the oxidative stress and affects the intracellular function of the cell. The ROS are very powerful oxidising agents ($^{\bullet}OH$, $^{\bullet}O_2^-$, and $HOO^{\bullet}$) which are not able to penetrate the cell wall and thus damage the organic molecules, such as lipids, nucleic acids, proteins, carbohydrates, DNA, and amino acids causing inhibition of cell growth.[24]

$$\text{Bacteria} + {}^{\bullet}OH \rightarrow \text{Inhibition of bacteria}$$

The positively charged Fe^{2+} and Fe^{3+} ions are also attracted by the negatively charged cellular proteins causing denaturation of proteins. Finally, microbial death resulted from diminished cell permeability, the ROS generation and protein deactivation triggered by nanomaterial interaction. Fig. 6 depicts an illustrative representation of the antibacterial mechanism.

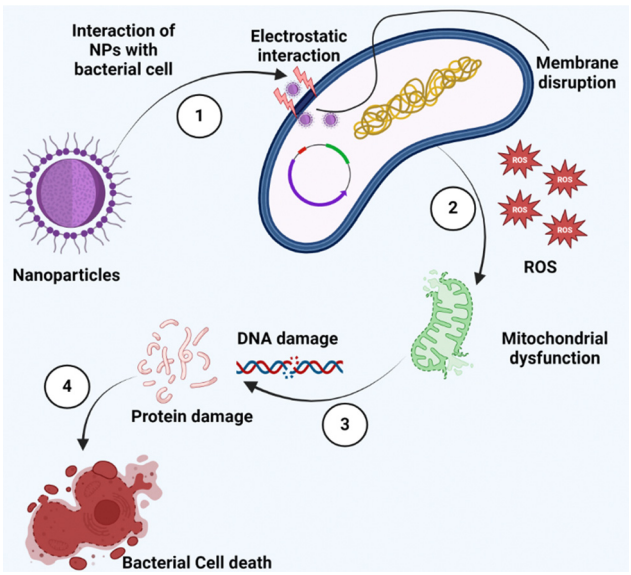

Fig. 6 Antibacterial mechanism of the OA-coated Fe_3O_4 NPs.

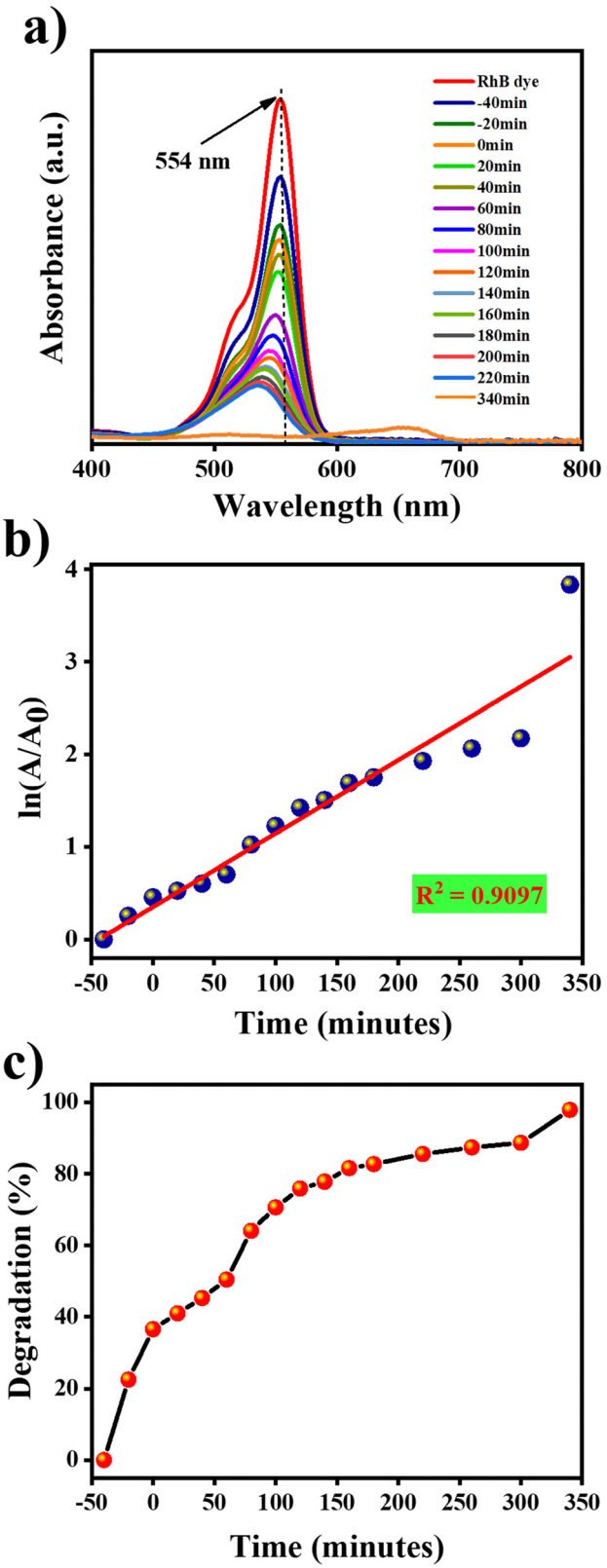

Fig. 7 (a) Absorbance spectra, (b) first order kinetic plot of $\ln(A/A_0)$ *vs.* time, (c) degradation efficiency of RhB dye using OA-coated Fe_3O_4 NPs.

Photocatalytic activity

The photocatalytic performance of OA-coated Fe_3O_4 NPs was evaluated by exposing them to visible light irradiation ($\lambda >$ 420 nm) and the absorption spectra were obtained at the wavelength of 554 nm (λ_{max}). (Fig. 7a) shows the UV-Vis absorption *vs.* time plot which indicated the decrease in absorption spectra of the RhB dye with the passage of time. Exposing the RhB dye solution to the OA-coated Fe_3O_4 NPs under visible light irradiation led to a progressive reduction in the absorbance intensity of the dye over time. Extending the visible light exposure to 340 minutes enhanced the degradation efficiency, achieving an impressive removal of approximately 99.17% of the RhB dye. This significant enhancement can be attributed to the OA functionalization, which reduces charge recombination by acting as a charge-separating layer, thereby extending the lifetime of excited charge carriers. The prolonged charge carrier separation facilitates higher ROS generation, which drives the degradation process more efficiently. The improved light absorption and charge transfer dynamics due to OA functionalization further contribute to the superior photocatalytic performance observed in our study. A comparative analysis of the photocatalytic efficiency of Fe_3O_4 NPs is provided in Table 4, reinforcing the impact of surface functionalization on enhanced degradation capability. The degradation rate kinetics of RhB dye in the presence of OA-coated Fe_3O_4 NPs was analyzed, and the slope of the kinetic curve was used to calculate the value of rate constant which came out to be 0.0079 min^{-1}. These results suggest that OA-coated Fe_3O_4 NPs exhibit high photocatalytic performance. While the OA coating primarily serves as a dispersing agent in the dye solution, the RhB dye itself interacts primarily with the hydrophobic hydrocarbon chain *i.e.* 'tail' of the OA molecule due to the strong attraction between the hydrocarbon chain and the dye's aromatic rings. Additionally, the observed degradation behavior follows a first-order kinetic model (shown in Fig. 7b), as described by eqn (9). Further, (Fig. 7c) demonstrates the achieved degradation efficiency of the dye after 340 minutes of exposure.

$$\ln\left(\frac{A}{A_0}\right) = kt \quad (9)$$

where A_0 and A are the initial and final absorbance at time 't' in minutes and k represents the rate constant.

Effect of catalyst dose

To investigate the effect of catalyst dose on the degradation efficiency of RhB dye, experiments were conducted using varying amounts of catalyst: 20 mg, 40 mg, 60 mg, and 80 mg.

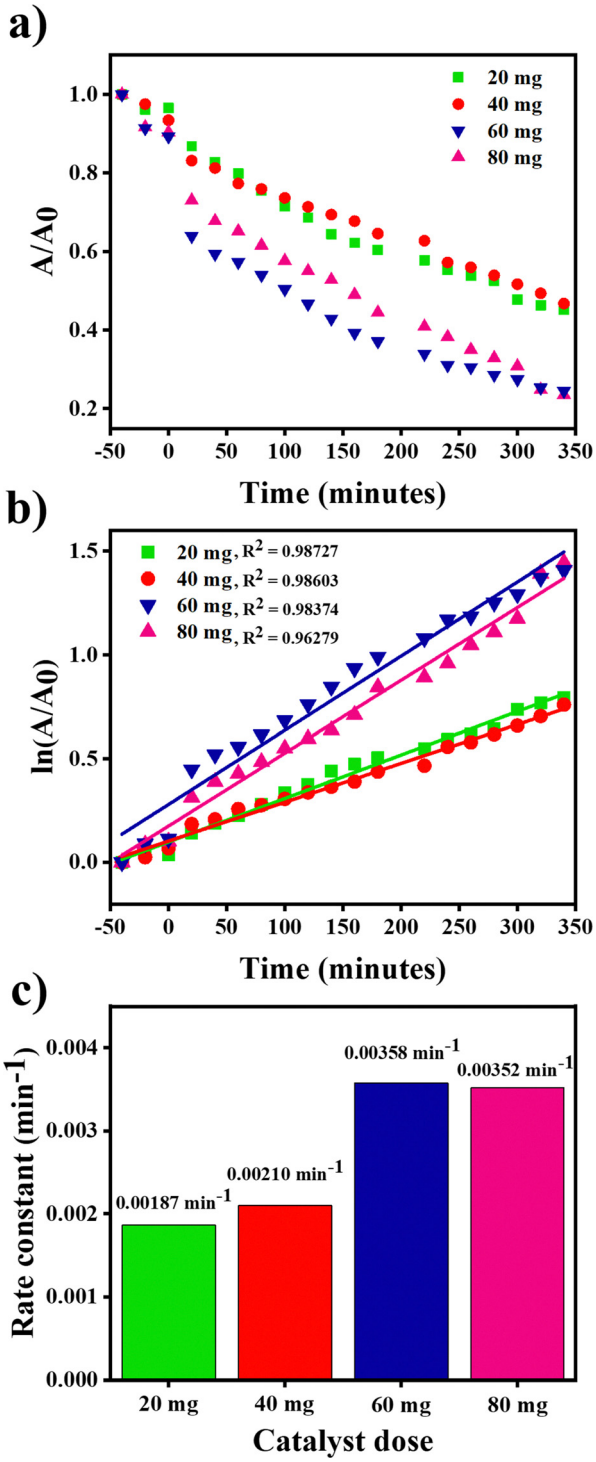

Fig. 8 (a) A/A_0 *vs.* time graph, (b) rate kinetics and (c) bar graph representing the rate constants at different catalyst dosage.

Table 4 Comparing the photocatalytic efficiency of Fe_3O_4 NPs

S. no.	Ferrite NPs	Source	Catalyst dose (g L^{-1})	Dye	Degradation (%)	Dye concentration (ppm)	Ref.
1	Fe_3O_4	Visible	0.4	RhB	23.8	5	74
2	Fe_3O_4	Visible	0.4	RhB	16	5	75
3	Fe_2O_3	Visible	1.25	RhB	38.03	24.25	76
4	Fe_3O_4	Visible	0.51	RhB	92.5	10	77
5	Fe_3O_4	Visible	1	RhB	~66	10	78
6	OA-coated Fe_3O_4	Visible lamp	1	RhB	99	10	[Present study]

The experiment was performed by taking the various amounts in 60 mL of dye solution each, with the dye concentration kept fixed. The results demonstrated the catalyst dose significantly influenced the photocatalytic degradation efficiency of the RhB dye. With increase in catalyst dose, the photocatalytic activity increased with higher catalyst dose, with the optimum degradation percentage observed at a catalyst dose of 60 mg. At catalyst dose of 20 mg and 40 mg, the degradation percentage of 53.23% and 54.81% and the maximum degradation of 76.44% was observed at 60 mg of catalyst dose. On further increasing the catalyst dose to 80 mg, the degradation percentage resulted in slight reduction showing 75.55% degradation efficiency. This trend can be explained by two factors. Initially, as the catalyst dose increases, more active sites become available, leading to a greater generation of electron–hole pairs, which in turn enhances the photocatalytic activity. However, at higher catalyst concentrations, particle–particle interactions result in a screening effect that reduces the penetration of photons to the photocatalyst surface. This shielding effect decreases the overall photodegradation efficiency, as fewer photons are available to initiate the photocatalytic reactions.[79] (Fig. 8a) illustrates the A/A_0 (absorbance ratio) *versus* time, depicting the rate kinetics of the photocatalyst at different dosages. First-order rate kinetics were applied, and the rate constants were calculated from the slopes of the fitted data, as shown in (Fig. 8b). The calculated rate constants for 20 mg, 40 mg, 60 mg, and 80 mg of catalyst are 0.00187 min^{-1}, 0.0021 min^{-1}, 0.00358 min^{-1}, and 0.00352 min^{-1}, respectively (shown in Fig. 8c). Based on these results, the optimal catalyst dose was chosen to be 60 mg, where the maximum degradation efficiency was observed.

Stability test

The stability and reusability of the OA-coated Fe_3O_4 NPs was tested by performing degradation experiments using RhB dye. After each cycle, the magnet was attached at the bottom of the beaker and solution was decanted. The resulted sample was washed multiple times in similar manner to desorb the adsorbed RhB dye, followed by drying in humidity chamber at 70 °C for subsequent cycles. The degradation activity was assessed by monitoring the photocatalytic degradation rate, revealing minimal reduction even after four consecutive cycles (as shown in Fig. 9a). The excellent reusability of OA-coated Fe_3O_4 NPs is attributed to the stability of their magnetic and surface properties, ensuring consistent performance across multiple cycles. The OA coating effectively prevents aggregation, preserves a high surface area, and stabilizes surface states essential for the efficient generation of ROS. This confirms that the NPs retain their photocatalytic activity due to preserved ROS generation and stable superparamagnetic behavior, making them highly effective for repeated applications. In addition, a morphological analysis of the material was conducted to evaluate any structural changes that might have occurred after the recyclability test. (Fig. 9b) presents the FESEM images of the NPs captured before and after conducting the degradation experiment after four consecutive cycles. The morphology of the NPs before the experiment is shown in (Fig. 9b), highlighting their initial structure and surface characteristics. (Fig. 9c) shows the NPs after four cycles of degradation experiment. A comparison of the images reveal no significant changes in the morphology or surface structure of the NPs after the recyclability test. This observation underscores the excellent photostability of the prepared functionalized sample, demonstrating its ability to maintain structural integrity and performance even after repeated use in photocatalytic degradation experiments. Such stability is a crucial attribute for the practical application of photocatalysts in long-term and sustainable pollutant degradation processes.

Fig. 10 illustrates the schematic representation of the photocatalytic mechanism of OA-coated Fe_3O_4 NPs. When a particular wavelength of visible light falls on the surface of OA-coated Fe_3O_4 NPs, the electron present in the VB absorbs that energy and gets excited to the CB which leads to the generation of electron–hole pairs. This photo-excited electron participates in redox reaction by reacting with the oxygen present in the atmosphere and results in producing superoxide radicals whereas the hole present in the valence band reacts with the water molecules present in the proximity of the solution resulting in producing •OH. These radicals further react with the molecules of RhB dye pollutant leading to the degradation of the dye molecules by producing carbon dioxide and water molecules.[58] Further, the enhancement in degradation percentage is mainly attributed to the additional •OH generated upon introducing H_2O_2.[77] This occurs through electron transfer from the conduction band of the photocatalyst to H_2O_2, creating

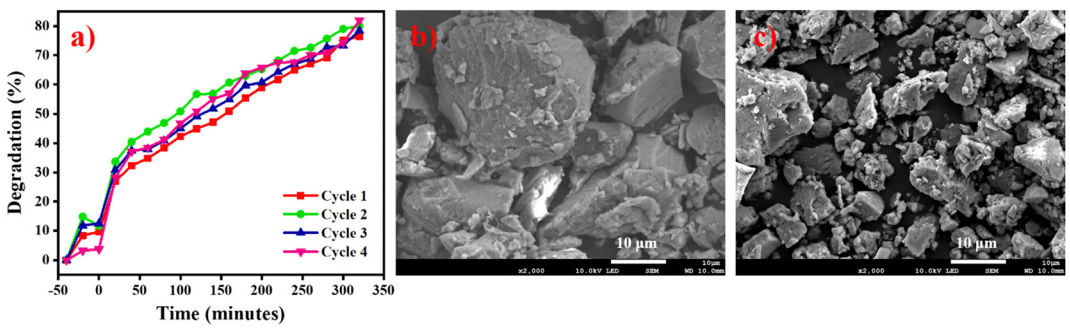

Fig. 9 (a) Stability test of the OA-coated Fe_3O_4 NPs as a photocatalyst, demonstrating their reusability over multiple cycles. (b) FESEM images of OA-coated Fe_3O_4 NPs showing the morphology before the degradation experiment and (c) after the recyclability test, highlighting structural changes.

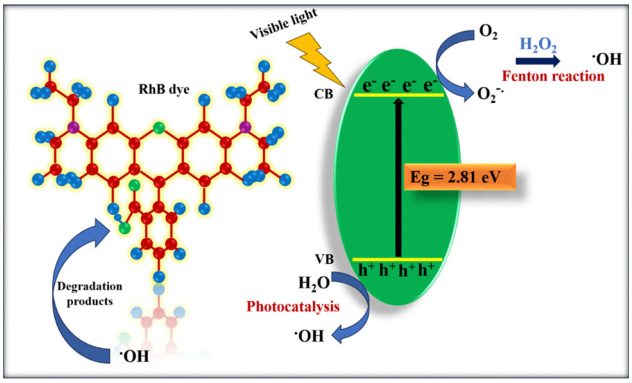

Fig. 10 Schematic representation of RhB dye degradation in presence of OA-coated Fe_3O_4 NPs under visible light irradiation.

highly reactive $^{\bullet}OH$ that intensify the overall degradation process. The possible dye degradation reactions are shown in eqn (10)–(16):

$$Fe_3O_4 + h\nu \rightarrow Fe_3O_4\,(e^- + h^+) \quad (10)$$

$$e^- + O_2 \rightarrow {}^{\bullet}O_2^- \quad (11)$$

$$h^+ + H_2O \rightarrow {}^{\bullet}OH \quad (12)$$

$$H_2O_2 + e^- \rightarrow OH^- + {}^{\bullet}OH \quad (13)$$

$$H_2O_2 + {}^{\bullet}O_2^- \rightarrow OH^- + {}^{\bullet}OH + O_2 \quad (14)$$

$${}^{\bullet}O_2^- + \text{Dye} \rightarrow \text{Degradation products} \quad (15)$$

$${}^{\bullet}OH + \text{Dye} \rightarrow \text{Degradation products} \quad (16)$$

Conclusion

In this study, OA coated-Fe_3O_4 NPs were synthesized *via* an eco-friendly and scalable co-precipitation method. Comprehensive characterization using XRD, FTIR, UV-Vis spectroscopy, HRTEM, and VSM confirmed the high crystallinity, effective functionalization, and robust magnetic properties of the synthesized NPs. XRD analysis revealed a single-phase cubic structure with a crystallite size of 12.17 nm, calculated using Debye–Scherrer's formula. FTIR and UV-Vis spectroscopy confirmed both the functionalization and optical properties of the samples. Furthermore, VSM analysis demonstrated the superparamagnetic nature of the NPs, with an M_s value of 34.80 emu g^{-1}. These multifunctional NPs exhibit superior antibacterial and photocatalytic activities, underscoring their dual applicability in biomedical and environmental domains. The antibacterial efficacy of the NPs was demonstrated through dose-dependent inhibition against *Escherichia coli* DH5α. At a concentration of 50 μg μL^{-1}, the NPs achieved a maximum ZOI of 9.28 mm, significantly outperforming similar ferrite-based systems reported in literature. This superior activity is attributed to the generation of ROS and the controlled release of Fe^{2+}/Fe^{3+} ions, which synergistically disrupt bacterial membranes, denature proteins, and damage genetic material. The role of OA in enhancing the dispersibility and interaction of NPs with microbial surfaces further amplifies their efficacy. The NPs also demonstrated remarkable photocatalytic degradation of RhB dye under visible light irradiation. Achieving 99.17% degradation within 340 minutes, the photocatalytic process follows first-order kinetics with a rate constant of 0.0079 min^{-1}. This exceptional performance is driven by the synergistic effects of OA coating on the Fe_3O_4 surface, which enhance charge separation, light absorption, and surface area availability. Furthermore, the magnetic recoverability of the NPs allowed efficient separation and reuse over four cycles, maintaining stability and performance, thus validating their economic and practical viability for environmental remediation. This work advances the understanding of multifunctional NPs, showcasing how surface functionalization can tailor their physicochemical properties to address critical global challenges. Overall, this study positions OA-coated Fe_3O_4 NPs as a potent, cost-effective solution for dual-action applications, bridging the gap between sustainable nanotechnology and real-world biomedical and environmental needs.

Author contributions

Shreya Sinha: conceptualization, methodology, investigation, data analysis, writing – original draft. Rahul Sharma: data analysis, investigation and writing – review & editing. Mohd Rehan Ansari: investigation, writing – review & editing. Rahul Singh: Investigation, Writing – Review & editing. Saurabh Pathak: data analysis, validation, supervision, writing – review & editing. Noor Jahan: resource, data analysis, validation, supervision, writing – review & editing. Koteswara Rao Peta: resource, writing – review & editing.

Data availability

The raw data supporting the findings of this study are available from the corresponding author upon reasonable request.

Conflicts of interest

The authors declare that there are no conflicts of interest regarding the publication of this manuscript.

Acknowledgements

The authors are grateful to Central University of Himachal Pradesh for financial support under UGC-BSR Project no. F. 30-581/2021 for providing the necessary research facilities for this work.

References

1 Y. Gao, K. Wang, J. Zhang, X. Duan, Q. Sun and K. Men, Multifunctional nanoparticle for cancer therapy, *MedComm*, 2023, **4**(1), e187, DOI: **10.1002/mco2.187**.

2 J. Gao, H. Gu and B. Xu, Multifunctional Magnetic Nanoparticles: Design, Synthesis, and Biomedical Applications, *Acc. Chem. Res.*, 2009, **42**(8), 1097–1107, DOI: **10.1021/ar9000026**.

3 S. Liu, B. Yu, S. Wang, Y. Shen and H. Cong, Preparation, surface functionalization and application of Fe_3O_4 magnetic nanoparticles, *Adv. Colloid Interface Sci.*, 2020, **281**, 102165, DOI: **10.1016/j.cis.2020.102165**.

4 R. Sharma, *et al.*, Doping stimulated ferromagnetic ordering and tailoring of the dielectric properties of $Ba_{1-x}Ce_xTiO_3$, *Mater. Adv.*, 2024, **5**(21), 8638–8651, DOI: **10.1039/D4MA00593G**.

5 N. Tabassum, D. Kumar, D. Verma, R. A. Bohara and M. P. Singh, Zirconium oxide (ZrO_2) nanoparticles from antibacterial activity to cytotoxicity: a next-generation of multifunctional nanoparticles, *Mater. Today Commun.*, 2021, **26**, 102156, DOI: **10.1016/j.mtcomm.2021.102156**.

6 K. Dulta, G. Koşarsoy Ağçeli, P. Chauhan, R. Jasrotia, P. K. Chauhan and J. O. Ighalo, Multifunctional CuO nanoparticles with enhanced photocatalytic dye degradation and antibacterial activity, *Sustainable Environ. Res.*, 2022, **32**(1), 2, DOI: **10.1186/s42834-021-00111-w**.

7 S. Ishwarya, *et al.*, Multifunctional, energy and environmental applications of calcium magnesium vanadate ($Ca_5Mg_4V_6O_{24}$) nanoparticles synthesized by solution combustion, *J. Appl. Electrochem.*, 2025, **55**, 357–376, DOI: **10.1007/s10800-024-02171-3**.

8 S. Sinha, R. Sharma, N. Jahan and P. R. Agrawal, Textile Tales: The Environmental Narrative of Fabrics and Fibers, in *Dye Pollution from Textile Industry: Challenges and Opportunities for Sustainable Development*, ed. P. Singh, Springer Nature, Singapore, 2024, pp. 405–422, DOI: **10.1007/978-981-97-5341-3_18**.

9 S. Sinha, N. Jahan and P. R. Agrawal, Dyes and Unveiling the Environmental Story of Dye Pollution, in *Dye Pollution from Textile Industry: Challenges and Opportunities for Sustainable Development*, ed. P. Singh, Springer Nature, Singapore, 2024, pp. 31–63, DOI: **10.1007/978-981-97-5341-3_3**.

10 L. Gabrielyan, H. Badalyan, V. Gevorgyan and A. Trchounian, Comparable antibacterial effects and action mechanisms of silver and iron oxide nanoparticles on *Escherichia coli* and *Salmonella typhimurium*, *Sci. Rep.*, 2020, **10**(1), 13145, DOI: **10.1038/s41598-020-70211-x**.

11 A. Nanda and M. Saravanan, Biosynthesis of silver nanoparticles from Staphylococcus aureus and its antimicrobial activity against MRSA and MRSE, *Nanomed. Nanotechnol. Biol. Med.*, 2009, **5**(4), 452–456, DOI: **10.1016/j.nano.2009.01.012**.

12 M. Mohapatra and S. Anand, Synthesis and applications of nano-structured iron oxides/hydroxides – a review, *Int. J. Eng. Sci. Technol.*, 2010, **2**(8), 127–146, DOI: **10.4314/ijest.v2i8.63846**.

13 S. Dabagh, S. A. Haris, B. K. Isfahani and Y. N. Ertas, Silver-Decorated and Silica-Capped Magnetite Nanoparticles with Effective Antibacterial Activity and Reusability, *ACS Appl. Bio Mater.*, 2023, **6**(6), 2266–2276, DOI: **10.1021/acsabm.3c00122**.

14 N. V. Jadhav, *et al.*, Synthesis of oleic acid functionalized Fe_3O_4 magnetic nanoparticles and studying their interaction with tumor cells for potential hyperthermia applications, *Colloids Surf., B*, 2013, **108**, 158–168, DOI: **10.1016/j.colsurfb.2013.02.035**.

15 M. D. Nguyen, H.-V. Tran, S. Xu and T. R. Lee, Fe_3O_4 Nanoparticles: Structures, Synthesis, Magnetic Properties, Surface Functionalization, and Emerging Applications, *Appl. Sci.*, 2021, **11**(23), 11301, DOI: **10.3390/app112311301**.

16 S. Pathak, *et al.*, Spin dynamics investigations of multifunctional ambient scalable Fe_3O_4 surface decorated ZnO magnetic nanocomposite using FMR, *Sci. Rep.*, 2021, **11**(1), 3799, DOI: **10.1038/s41598-021-83394-8**.

17 N. Jahan, S. Pathak, K. Jain and R. P. Pant, Enchancment in viscoelastic properties of flake-shaped iron based magnetorheological fluid using ferrofluid, *Colloids Surf., A*, 2017, **529**, 88–94, DOI: **10.1016/j.colsurfa.2017.05.057**.

18 R. Singh, S. Pathak, K. Jain and S.-K. Kim, Correlating the Dipolar Interactions Induced Magneto-Viscoelasticity and Thermal Conductivity Enhancements in Nanomagnetic Fluids, *Small*, 2023, **19**(39), 2205741, DOI: **10.1002/smll.202205741**.

19 M. S. Sharif, *et al.*, Biofabrication of Fe_3O_4 Nanoparticles from Spirogyra hyalina and Ajuga bracteosa and Their Antibacterial Applications, *Molecules*, 2023, **28**(8), 3403, DOI: **10.3390/molecules28083403**.

20 B. Kumar, K. Smita, L. Cumbal, A. Debut, S. Galeas and V. H. Guerrero, Phytosynthesis and photocatalytic activity of magnetite (Fe_3O_4) nanoparticles using the Andean blackberry leaf, *Mater. Chem. Phys.*, 2016, **179**, 310–315, DOI: **10.1016/j.matchemphys.2016.05.045**.

21 R. Haghniaz, *et al.*, Anti-bacterial and wound healing-promoting effects of zinc ferrite nanoparticles, *J. Nanobiotechnol.*, 2021, **19**(1), 38, DOI: **10.1186/s12951-021-00776-w**.

22 L. S. Ganapathe, M. A. Mohamed, R. Mohamad Yunus and D. D. Berhanuddin, Magnetite (Fe_3O_4) Nanoparticles in Biomedical Application: From Synthesis to Surface Functionalisation, *Magnetochemistry*, 2020, **6**(4), 68, DOI: **10.3390/magnetochemistry6040068**.

23 M. Alavi and N. Karimi, Ultrasound assisted-phytofabricated Fe_3O_4 NPs with antioxidant properties and antibacterial effects on growth, biofilm formation, and spreading ability of multidrug resistant bacteria, *Artif. Cells, Nanomed., Biotechnol.*, 2019, **47**(1), 2405–2423, DOI: **10.1080/21691401.2019.1624560**.

24 R. Tiwari, M. De, H. S. Tewari and S. K. Ghoshal, Structural and magnetic properties of tailored $NiFe_2O_4$ nanostructures synthesized using auto-combustion method, *Results Phys.*, 2020, **16**, 102916, DOI: **10.1016/j.rinp.2019.102916**.

25 M. M. Naik, H. S. B. Naik, N. Kottam, M. Vinuth, G. Nagaraju and M. C. Prabhakara, Multifunctional properties of microwave-assisted bioengineered nickel doped cobalt ferrite nanoparticles, *J. Sol-Gel Sci. Technol.*, 2019, **91**(3), 578–595, DOI: **10.1007/s10971-019-05048-6**.

26 M. R. Ansari, A. Kem, P. Agrohi, P. K. Mallick, P. Rao and K. R. Peta, Structural, optical, magnetic and anti-bacterial

properties of green synthesized spinel zinc ferrite by microwave-assisted method, *Mater. Chem. Phys.*, 2023, **301**, 127641, DOI: 10.1016/j.matchemphys.2023.127641.

27 S. Dabagh, S. A. Haris and Y. N. Ertas, Synthesis, Characterization and Potent Antibacterial Activity of Metal-Substituted Spinel Ferrite Nanoparticles, *J. Cluster Sci.*, 2023, **34**(4), 2067–2078, DOI: 10.1007/s10876-022-02373-9.

28 M. A. Sharpe, S. J. Robb and J. B. Clark, Nitric oxide and Fenton/Haber–Weiss chemistry: nitric oxide is a potent antioxidant at physiological concentrations, *J. Neurochem.*, 2003, **87**(2), 386–394, DOI: 10.1046/j.1471-4159.2003.02001.x.

29 J. Singh, *et al.*, Experimental and first-principle insight into Structural, optical and electrical properties and photocatalytic water purification application of $Zn_{1-x}Mg_xO$, *Inorg. Chem. Commun.*, 2024, **162**, 112238, DOI: 10.1016/j.inoche.2024.112238.

30 L. Velayutham, *et al.*, Photocatalytic and Antibacterial Activity of $CoFe_2O_4$ Nanoparticles from Hibiscus rosa-sinensis Plant Extract, *Nanomaterials*, 2022, **12**(20), 3668, DOI: 10.3390/nano12203668.

31 A. I. Saber, *et al.*, Efficient photocatalytic degradation of tetracycline antibiotic and melachite green dye using La-BDC MOFs, *Emergent Mater.*, 2024, **7**(3), 1019–1030, DOI: 10.1007/s42247-024-00644-x.

32 K. Hatami, Z. Baghbantaraghdari, D. Jamaledin, F. Dabbagh Moghaddam, N. Kaneko and M. Ghovvati, Synthesis Characterization Antioxidant and Antibacterial Activities of Zinc Ferrite and Copper Ferrite Nanoparticles, *Mater. Chem. Horiz.*, 2023, **2**(1), 49–56, DOI: 10.22128/mch.2022.613.1030.

33 M. M. Naik, H. S. B. Naik, G. Nagaraju, M. Vinuth, K. Vinu and S. K. Rashmi, Effect of aluminium doping on structural, optical, photocatalytic and antibacterial activity on nickel ferrite nanoparticles by sol–gel auto-combustion method, *J. Mater. Sci.: Mater. Electron.*, 2018, **29**(23), 20395–20414, DOI: 10.1007/s10854-018-0174-y.

34 R. Rahmayeni, Y. Oktavia, Y. Stiadi, S. Arief and Z. Zulhadjri, Spinel ferrite of $MnFe_2O_4$ synthesized in *Piper betle* Linn extract media and its application as photocatalysts and antibacterial, *J. Dispers. Sci. Technol.*, 2021, **42**(3), 465–474, DOI: 10.1080/01932691.2020.1721011.

35 R. Anusa, C. Ravichandran, T. V. Rajendran, M. V. Arularasu and E. K. T. Sivakumar, Comparative investigation of cobalt ferrite ($CoFe_2O_4$) and cadmium ferrite ($CdFe_2O_4$) nanoparticles for the structural, optical properties and antibacterial activity, *Digest J. Nanomater. Biostruct.*, 2019, **14**(2), 367–374.

36 M. Ikram, *et al.*, Toward Efficient Bactericidal and Dye Degradation Performance of Strontium- and Starch-Doped Fe_2O_3 Nanostructures: In Silico Molecular Docking Studies, *ACS Omega*, 2023, **8**(8), 8066–8077, DOI: 10.1021/acsomega.2c07980.

37 Y. T. Prabhu, K. V. Rao, B. S. Kumari, V. S. S. Kumar and T. Pavani, Synthesis of Fe_3O_4 nanoparticles and its antibacterial application, *Int. Nano Lett.*, 2015, **5**(2), 85–92, DOI: 10.1007/s40089-015-0141-z.

38 R. Verma, J. Gangwar and A. K. Srivastava, Multiphase TiO_2 nanostructures: a review of efficient synthesis, growth mechanism, probing capabilities, and applications in biosafety and health, *RSC Adv.*, 2017, **7**(70), 44199–44224, DOI: 10.1039/C7RA06925A.

39 J. Gaur, *et al.*, Photocatalytic degradation of Congo red dye using zinc oxide nanoparticles prepared using Carica papaya leaf extract, *Mater. Today Sustain.*, 2023, **22**, 100339, DOI: 10.1016/j.mtsust.2023.100339.

40 Parul, K. Kaur, R. Badru, P. P. Singh and S. Kaushal, Photodegradation of organic pollutants using heterojunctions: a review, *J. Environ. Chem. Eng.*, 2020, **8**(2), 103666, DOI: 10.1016/j.jece.2020.103666.

41 H. C. Diogo, M. Melhem, A. Sarpieri and M. C. Pires, Avaliação do método de disco-difusão para determinação da eficácia da terbinafina in vitro em agentes de micoses superficiais e subcutâneas, *An. Bras. Dermatol.*, 2010, **85**(3), 324–330, DOI: 10.1590/S0365-05962010000300005.

42 X. Wu and Z. Nan, Degradation of rhodamine B by a novel Fe_3O_4/SiO_2 double-mesoporous-shelled hollow spheres through photo-Fenton process, *Mater. Chem. Phys.*, 2019, **227**, 302–312, DOI: 10.1016/j.matchemphys.2019.02.023.

43 M. Utami, *et al.*, Photocatalytic degradation of rhodamine B dye pollutants by Fe_3O_4/SiO_2 core–shell magnetic nanocomposite functionalized with TiO_2, *Environ. Geochem. Health*, 2024, **46**(10), 378, DOI: 10.1007/s10653-024-02165-2.

44 L. Han, X. Zhou, L. Wan, Y. Deng and S. Zhan, Synthesis of $ZnFe_2O_4$ nanoplates by succinic acid-assisted hydrothermal route and their photocatalytic degradation of rhodamine B under visible light, *J. Environ. Chem. Eng.*, 2014, **2**(1), 123–130, DOI: 10.1016/j.jece.2013.11.031.

45 A. Manohar, K. Chintagumpala and K. H. Kim, Magnetic hyperthermia and photocatalytic degradation of rhodamine B dye using Zn-doped spinel Fe_3O_4 nanoparticles, *J. Mater. Sci.: Mater. Electron.*, 2021, **32**(7), 8778–8787, DOI: 10.1007/s10854-021-05549-7.

46 X. Xu, Strong Visible Light Photocatalytic Activity of Magnetically Recyclable Sol–Gel-Synthesized $ZnFe_2O_4$ for Rhodamine B, *J. Electron. Mater.*, 2018, **47**(1), 536–541, DOI: 10.1007/s11664-017-5810-4.

47 M. R. Ansari, P. Agrohi and K. R. Peta, Effect of citric acid on structural, optical, morphological properties of ZnO and the bactericidal applications against human pathogenic bacteria *E. coli* DH5α, *Mater. Today Proc*, 2024, DOI: 10.1016/j.matpr.2024.01.009.

48 S. Shreya, S. Rahul, S. Rahul, J. Noor and K. Jasmeet, Synthesis, Characterization and Photocatalytic Application of GO/Fe_3O_4 Nanocomposite, *Recent Advances in Nanomaterials*, Springer Nature Singapore, Singapore, 2024, pp. 525–530.

49 Z. Karcıoğlu Karakaş, R. Boncukcuoğlu, İ. H. Karakaş and M. Ertuğrul, The effects of heat treatment on the synthesis of nickel ferrite ($NiFe_2O_4$) nanoparticles using the microwave assisted combustion method, *J. Magn. Magn. Mater.*, 2015, **374**, 298–306, DOI: 10.1016/j.jmmm.2014.08.045.

50 R. Tiwari, M. De, H. S. Tewari and S. K. Ghoshal, Structural and magnetic properties of tailored $NiFe_2O_4$ nanostructures synthesized using auto-combustion method, *Results Phys.*, 2020, **16**, 102916, DOI: 10.1016/j.rinp.2019.102916.

51 N. Kumar, *et al.*, $NiFe_2O_4$ nanoparticles as highly efficient catalyst for oxygen reduction reaction and energy storage in supercapacitor, *Mater. Chem. Phys.*, 2024, 129072.
52 A. Gholizadeh, A comparative study of physical properties in Fe_3O_4 nanoparticles prepared by coprecipitation and citrate methods, *J. Am. Ceram. Soc.*, 2017, **100**(8), 3577–3588, DOI: 10.1111/jace.14896.
53 G. Herrera-Perez, J. Plaisier, A. Reyes-Rojas and L. Fuentes-Cobas, Electron density contour maps via Rietveld-MEM analysis using HR-XRD for the polycrystalline ferroelectric BCZT, *Supl. Rev. Mex. Física*, 2022, **3**(1), DOI: 10.31349/SuplRevMexFis.3.010601.
54 T. F. Marinca, *et al.*, Mechanosynthesis, structural, thermal and magnetic characteristics of oleic acid coated Fe_3O_4 nanoparticles, *Mater. Chem. Phys.*, 2016, **171**, 336–345, DOI: 10.1016/j.matchemphys.2016.01.025.
55 Y. A. Urian, J. J. Atoche-Medrano, L. T. Quispe, L. León Félix and J. A. H. Coaquira, Study of the surface properties and particle-particle interactions in oleic acid-coated Fe_3O_4 nanoparticles, *J. Magn. Magn. Mater.*, 2021, **525**, 167686, DOI: 10.1016/j.jmmm.2020.167686.
56 Q. Lan, C. Liu, F. Yang, S. Liu, J. Xu and D. Sun, Synthesis of bilayer oleic acid-coated Fe_3O_4 nanoparticles and their application in pH-responsive Pickering emulsions, *J. Colloid Interface Sci.*, 2007, **310**(1), 260–269, DOI: 10.1016/j.jcis.2007.01.081.
57 T. Malaeru, *et al.*, Preparation and Characterization of Fe_3O_4 Magnetic Nanofluid in Vegetable Oil, *Rev. Chim.*, 2019, **70**(2), 459–464, DOI: 10.37358/RC.19.2.6935.
58 H. Keshavarz, A. Khavandi, S. Alamolhoda and M. R. Naimi-Jamal, pH-Sensitive magnetite mesoporous silica nanocomposites for controlled drug delivery and hyperthermia, *RSC Adv.*, 2020, **10**(64), 39008–39016, DOI: 10.1039/D0RA06916G.
59 K. Bootdee, B. P. Grady and M. Nithitanakul, Magnetite/poly(D,L-lactide-*co*-glycolide) and hydroxyapatite/poly(D,L-lactide-*co*-glycolide) prepared by w/o/w emulsion technique for drug carrier: physical characteristic of composite nanoparticles, *Colloid Polym. Sci.*, 2017, **295**(10), 2031–2040, DOI: 10.1007/s00396-017-4185-7.
60 R. Ghosh, *et al.*, Induction heating studies of Fe_3O_4 magnetic nanoparticles capped with oleic acid and polyethylene glycol for hyperthermia, *J. Mater. Chem.*, 2011, **21**(35), 13388, DOI: 10.1039/c1jm10092k.
61 M. Mahdavi, *et al.*, Synthesis, Surface Modification and Characterisation of Biocompatible Magnetic Iron Oxide Nanoparticles for Biomedical Applications, *Molecules*, 2013, **18**(7), 7533–7548, DOI: 10.3390/molecules18077533.
62 L. P. Mona, S. P. Songca and P. A. Ajibade, Effects of Temperature and Precursor Concentration on the Morphological and Optical Properties of Iron Oxide Nanoparticles, *Chem. Afr.*, 2024, **7**(8), 4581–4591, DOI: 10.1007/s42250-024-01057-3.
63 I. P. T. Indrayana, Synthesis, characterization, and application of Fe_3O_4 nanoparticles as a signal amplifier element in surface plasmon resonance biosensing, *J. Online Phys.*, 2020, **5**(2), 65–74, DOI: 10.22437/jop.v5i2.8259.
64 M. M. Rahman, M. M. Hussain and A. M. Asiri, Fabrication of 3-methoxyphenol sensor based on Fe_3O_4 decorated carbon nanotube nanocomposites for environmental safety: real sample analyses, *PLoS One*, 2017, **12**(9), e0177817, DOI: 10.1371/journal.pone.0177817.
65 T. Muthukumaran and J. Philip, Effect of phosphate and oleic acid capping on structure, magnetic properties and thermal stability of iron oxide nanoparticles, *J. Alloys Compd.*, 2016, **689**, 959–968, DOI: 10.1016/j.jallcom.2016.08.067.
66 M. Świętek, *et al.*, Magnetic Temperature-Sensitive Solid–Lipid Particles for Targeting and Killing Tumor Cells, *Front. Chem.*, 2020, **8**, 205, DOI: 10.3389/fchem.2020.00205.
67 H. Wu, L. Hao, C. Chen and J. Zhou, Superhydrophobic Fe_3O_4/OA Magnetorheological Fluid for Removing Oil Slick from Water Surfaces Effectively and Quickly, *ACS Omega*, 2020, **5**(42), 27425–27432, DOI: 10.1021/acsomega.0c03857.
68 P. Kumar, H. Khanduri, S. Pathak, A. Singh, G. A. Basheed and R. P. Pant, Temperature selectivity for single phase hydrothermal synthesis of PEG-400 coated magnetite nanoparticles, *Dalton Trans.*, 2020, **49**(25), 8672–8683, DOI: 10.1039/D0DT01318H.
69 P. B. Shete, R. M. Patil, B. M. Tiwale and S. H. Pawar, Water dispersible oleic acid-coated Fe_3O_4 nanoparticles for biomedical applications, *J. Magn. Magn. Mater.*, 2015, **377**, 406–410, DOI: 10.1016/j.jmmm.2014.10.137.
70 S. Mohapatra, N. Pramanik, S. K. Ghosh and P. Pramanik, Synthesis and Characterization of Ultrafine Poly(vinyl-alcohol phosphate) Coated Magnetite Nanoparticles, *J. Nanosci. Nanotechnol.*, 2006, **6**(3), 823–829, DOI: 10.1166/jnn.2006.117.
71 S. Pathak, *et al.*, OPEN Spin dynamics investigations, *Sci. Rep.*, 2021, **11**, DOI: 10.1038/s41598-021-83394-8.
72 P. Kumar, *et al.*, Observation of intrinsic fluorescence in cobalt ferrite magnetic nanoparticles by Mn^{2+} substitution and tuning the spin dynamics by cation distribution, *J. Mater. Chem. C*, 2022, **10**(35), 12652–12679.
73 S. Kaur, *et al.*, Spinel nanoferrite ($CoFe_2O_4$): the impact of Cr doping on its structural, surface morphology, magnetic, and antibacterial activity traits, *Opt. Mater.*, 2022, **133**, 113026, DOI: 10.1016/j.optmat.2022.113026.
74 M. Shekofteh-Gohari and A. Habibi-Yangjeh, Fe_3O_4/ZnO/$CoWO_4$ nanocomposites: novel magnetically separable visible-light-driven photocatalysts with enhanced activity in degradation of different dye pollutants, *Ceram. Int.*, 2017, **43**(3), 3063–3071, DOI: 10.1016/j.ceramint.2016.11.115.
75 M. Shekofteh-Gohari and A. Habibi-Yangjeh, Fabrication of novel magnetically separable visible-light-driven photocatalysts through photosensitization of Fe_3O_4/ZnO with $CuWO_4$, *J. Ind. Eng. Chem.*, 2016, **44**, 174–184, DOI: 10.1016/j.jiec.2016.08.028.
76 P. C. L. Muraro, *et al.*, Iron oxide nanocatalyst with titanium and silver nanoparticles: synthesis, characterization and photocatalytic activity on the degradation of Rhodamine B dye, *Sci. Rep.*, 2020, **10**(1), 3055, DOI: 10.1038/s41598-020-59987-0.

77 S. K. Giri and N. N. Das, Visible light induced photocatalytic decolourisation of rhodamine B by magnetite nanoparticles synthesised using recovered iron from waste iron ore tailing, *Desalination Water Treat.*, 2016, **57**(2), 900–907, DOI: **10.1080/19443994.2014.972984**.

78 M. S. Ansari, K. Raees, M. Ali Khan, M. Z. A. Rafiquee and M. Otero, Kinetic Studies on the Catalytic Degradation of Rhodamine B by Hydrogen Peroxide: Effect of Surfactant Coated and Non-Coated Iron(III) Oxide Nanoparticles, *Polymers*, 2020, **12**(10), 2246, DOI: **10.3390/polym12102246**.

79 A. R. Bhapkar, *et al.*, Aluminium doped ZnO nanostructures for efficient photodegradation of indigo carmine and azo carmine G in solar irradiation, *Appl. Nanosci.*, 2023, **13**(8), 5777–5793, DOI: **10.1007/s13204-023-02824-3**.